Applied Catalysis B: Environmental 129 (2013) 255–263

Contents lists available at SciVerse ScienceDirect

Applied Catalysis B: Environmental

journal homepage: www.elsevier.com/locate/apcatb

Synthesis of g-C_3N_4/$SmVO_4$ composite photocatalyst with improved visible light photocatalytic activities in RhB degradation

Tingting Li[c], Leihong Zhao[c], Yiming He[b,*], Jun Cai[b], Mengfei Luo[c], Jianjun Lin[a,*]

[a] College of Chemical and Life Science, Zhejiang Normal University, Jinhua 321004, China
[b] Department of Materials Physics, Zhejiang Normal University, Jinhua 321004, China
[c] Institute of Physical Chemistry, Zhejiang Key Laboratory for Reactive Chemistry on Solid Surfaces, Zhejiang Normal University, Jinhua 321004, China

ARTICLE INFO

Article history:
Received 5 July 2012
Received in revised form
16 September 2012
Accepted 19 September 2012
Available online 28 September 2012

Keywords:
Photocatalytic activity
g-C_3N_4
$SmVO_4$
Photoluminescence

ABSTRACT

This paper reported novel graphitic carbon nitride (g-C_3N_4) and $SmVO_4$ composite photocatalysts which were prepared through a simple mixing–calcination method. Multiple techniques, such as Brunauer–Emmett–Teller (BET) method, thermogravimetric/differential thermal analysis (TG–DTA), X-ray diffraction (XRD), Fourier transform infrared (FT-IR) spectroscopy, scanning electron microscopy (SEM), transmission electron microscopy (TEM), X-ray photoelectron spectroscopy (XPS), UV–vis diffuse reflectance spectroscopy (DRS), and photoluminescence (PL) spectroscopy were applied to investigate the physical and photophysical properties of the catalysts. The XRD and FT-IR results indicate that the prepared sample is a two-phase composite of $SmVO_4$ and g-C_3N_4. The TG–DTA result suggests that the real g-C_3N_4 concentration in the composite is lower than the theoretical value due to the catalysis of $SmVO_4$. The DRS result shows that the addition of $SmVO_4$ to g-C_3N_4 slightly changes the optical properties. The photocatalytic activity of the novel composite was investigated using rhodamine B (RhB) as a target pollutant. Results show that the g-C_3N_4/$SmVO_4$ photocatalysts exhibit a significantly enhanced photocatalytic activity in degrading RhB. The optimal $SmVO_4$ concentration and calcination temperature were also determined. Based on the band position, the synergetic effect of $SmVO_4$ and g-C_3N_4 is the source of the enhanced photocatalytic activity, as proven by PL spectroscopy and transient photocurrent response.

1. Introduction

Photocatalysis using semiconductor has received considering interest in both scientific and engineering areas since 1972. The photogenerated holes and electrons are essentially oxidation and reduction species, respectively. Therefore, semiconductor photocatalysts with strong oxidation–reduction power have been widely studied for environment cleaning and for hydrogen generation from water splitting [1–3]. TiO_2 is considered as the one of the best photocatalyst due to its non-toxicity, good stability and excellent photocatalytic activity. However, TiO_2 is only responsive to ultraviolet light because of its wide band gap, which occupies no more than 4% of the solar spectrum. In view of the better utilization of solar light, it is appealing to develop visible light-sensitive photocatalysts that are active enough for practical applications.

Two strategies are generally applied to develop visible-light driven photocatalysts. One method is the modification of TiO_2 by metal-ion (such as Fe, Co, and W) doping [4,5], non-metal (such as N, C, S, and H) doping [6–9], and dye sensitization [10]. Another method is the development of new and efficient visible-light sensitive semiconductors. Recently, numerous investigations on novel visible-light driven photocatalyst have been undertaken. Several novel photocatalysts have been developed, such as AgBr, BiOX (X = Br, I), Ag_3PO_4, TaON, and $CaBi_6O_{10}$ [11–16]. Among the novel semiconductors, the Ag_3PO_4 photocatalyst has the highest photocatalytic activity with 90% quantum efficiency [16]. However, it is too expensive to be applied in practice. Actually, many semiconductor photocatalysts are confronted with the same problem since nearly all novel photocatalysts contain a metal element which increases the cost of photocatalyst. Different from metal-oxide photocatalysts, the graphite-like carbon nitride (g-C_3N_4) is a metal-free semiconductor composed of carbon and nitrogen only. It can be prepared by the simple heating of urea and melamine at 500 °C to 600 °C [17,18]. Therefore, g-C_3N_4 is inexpensive and is considered as a "sustainable" photocatalyst. The band gap is 2.70 eV, indicating that g-C_3N_4 can absorb visible light. Besides, g-C_3N_4 semiconductor is stable in solutions with pH = 0–14 under light irradiation. These superior properties imply that the metal-free g-C_3N_4 has numerous potential applications in the field of photocatalysis. However, the photoactivity of g-C_3N_4 is low compared with

* Corresponding authors. Tel.: +86 0579 83792294; fax: +86 0579 83714946.
E-mail addresses: hym@zjnu.cn (Y. He), linjj@zjnu.cn (J. Lin).

0926-3373/$ – see front matter © 2012 Elsevier B.V. All rights reserved.
http://dx.doi.org/10.1016/j.apcatb.2012.09.031

photocatalysts with high activity, such as Ag_3PO_4 and Ag/AgCl. To resolve this problem, attempts have been made to improve the photocatalytic performance of g-C_3N_4 [19–22]. Liu et al. reported that sulfur doping in g-C_3N_4 can markedly change the electron structure [19]. The synthesized S-doped g-C_3N_4 shows a photoreactivity of H_2 evolution that is 7.2 and 8.0 times higher than that of g-C_3N_4 under $\lambda > 300$ and 420 nm, respectively. Zhang et al. reported that g-C_3N_4 could be reversibly protonated by strong mineral acids, thus modifying its solubility, dispersability, electronic structure, and increasing its surface area [20]. The H_2 production efficacy of the proton-activated g-C_3N_4 in visible light is increased by a factor of 2. The construction of the heterojunction between g-C_3N_4 and another semiconductor with suitable band potential is also a feasible route to improve the photocatalytic activity. Yan et al. reported an organic–inorganic composite photocatalyst of g-C_3N_4/TaON that shows a higher activity than either the single-phase g-C_3N_4 or TaON in RhB photodegradation [21]. The coupling of N-doped In_2TiO_5 and Bi_2WO_6 can also promote the photocatalytic activity of g-C_3N_4 [22,23].

Orthovanadates are widely used as oxidation catalysts for dehydrogenation, ethanol-detecting sensors, and counter electrodes in electrochromic devices due to their interesting optical, catalytic, electrical and magnetic properties [24–27]. Orthovanadates are also possible candidates as photocatalytic material [28,29]. However, the introduced metal cation greatly affects the electron structure of vanadate salts, which subsequently influences the photocatalytic performance and optical properties. For example, YVO_4 has a high photocatalytic activity but could only absorb ultraviolet (UV) light [30], whereas $LaVO_4$ displays poor photocatalytic activity but has superior photoabsorption properties [31,32]. Only a portion of vanadate salts with suitable band structure has good photocatalytic activity under visible light irradiation, and exhibits great potential in the field of photocatalysis. The best representative is $BiVO_4$. Many $BiVO_4$-based composites are efficient photocatalysts [33–35]. Just like $BiVO_4$, $SmVO_4$ which has good activity for acetone degradation under visible light irradiation can be a highly efficient photocatalyst [36]. However, only a few studies on improvement of the photocatalytic activity of $SmVO_4$ have been performed. In the present study, the preparation of a novel composite material comprising $SmVO_4$ and g-C_3N_4 is reported for the first time. This g-C_3N_4/$SmVO_4$ composite exhibits strong photocatalytic activity for RhB decomposition and high photocatalytic stability under visible light irradiation.

2. Experimental

2.1. Preparation of catalysts

NH_4VO_3 (>99%), Sm_2O_3 (>99.9%), melamine (99%), tetrabutyl titanate (>99.0%), urea (99%), and ethanol (>99.5%) were purchased commercially and used without further purification. Pure $SmVO_4$ was prepared by precipitation method: Solutions of NH_4VO_3 and $Sm(NO_3)_3$ (obtained by dissolving Sm_2O_3 in HNO_3 solution) with a V to Sm mole ratio of 1:1 were mixed to give a deposit. The pH value of the solution was adjusted to 7 by a solution of NH_3. After aged at room temperature for 2 h, the deposit was filtered, washed three times by water, dried at 100 °C for 12 h and calcined at 500 °C for 2 h.

Pure g-C_3N_4 powders were prepared by directing calcining melamine in a muffle furnace. In a typical synthesis run, 6 g of melamine was placed in a semi-closed alumina crucible with a cover. The crucible was heated to 520 °C for 4 h with a heating rate of 10 °C/min. After cooling to room temperature, g-C_3N_4 was obtained in a powder form.

The g-C_3N_4/$SmVO_4$ composite was prepared according to the following procedure. 0.30 g of $SmVO_4$ and 0.70 g of g-C_3N_4 were mixed and ground in an agate mortar for 20 min. Then, the mixture was calcined at 500 °C for 2 h to obtain the 70 wt.% g-C_3N_4/$SmVO_4$ catalyst. Other g-C_3N_4/$SmVO_4$ catalysts were prepared by a similar method, only the g-C_3N_4 concentration or the calcination temperature was changed. In order to make clarity, the synthesized g-C_3N_4/$SmVO_4$ composites are denoted as *x* wt.% CS-*T*. Herein, *x* represents the g-C_3N_4 concentration and *T* represents the calcination temperature. For example, the 70 wt.% g-C_3N_4/$SmVO_4$ catalyst calcined at 450 °C can be denoted as 70 wt.% CS-450.

N-doped TiO_2 (N-TiO_2) was prepared by a modified sol–gel method. 8.0 mL of tetrabutyl titanate was dissolved in 48 mL of ethanol to obtain solution A. 5.65 g urea was dissolved in 8.0 mL H_2O and 24 mL ethanol to obtain solution B. Solution B was dropped slowly into solution A under stirring to form a sol. The sol was then transformed into a gel after aging for 12 h. Finally, the gel was dried at 80 °C and calcined at 500 °C for 3 h to obtain a yellow product.

2.2. Photocatalytic experiments

The photocatalytic activities of the synthesized powders were evaluated by the degradation of 10 mg/L RhB under visible-light irradiation. The light source for photocatalysis was a spherical Xe lamp (350 W). Two optical filters were used to eliminate the UV light ($\lambda < 420$ nm) and infrared light ($\lambda > 800$ nm). The power density at the position of reactor is about 7.3 mW/cm^2. In each experiment, 0.30 g of photocatalyst was added to 300 mL of RhB solution. Prior to irradiation, the suspension was magnetically stirred in the dark for an hour to ensure adsorption/desorption equilibrium at room temperature. At regular intervals, samples were withdrawn and centrifuged to separate solid particles for analysis. The concentration of aqueous RhB was determined using a UV–vis spectrophotometer at 554 nm by measuring its absorbance. The RhB degradation was calculated by Lambert–Beer equation. Photoactivities for RhB in the dark in the presence of the photocatalyst and under visible-light irradiation in the absence of the photocatalyst were also evaluated.

2.3. Characterizations

The thermogravimetry and differential thermal analysis (TG–DTA) curves were recorded on Netzsch STA449 thermal analysis instruments under the flow of air gas at a heating rate of 10 °C/min. The specific surface areas were measured on Autosorb-1 (Quantachrome Instruments) by the Brunauer–Emmett–Teller (BET) method. The morphology of the samples was characterized by scanning electron microscope (Nanoscope IIIa) and transmission electron microscopy (Hitachi S-4800). The crystal structure of the samples was investigated using an X-ray diffractometer (XRD, Philips PW3040/60) with Cu Kα radiation. The structural information for the samples was measured by Fourier transform spectrophotometer (FT-IR, Nicolet NEXUS670) with KBr as the reference sample. The surface information of the samples was investigated by X-ray photoelectron spectroscopy (XPS, Quantum 2000 Scanning ESCA Microprobe instrument). The C 1s signal was set to a position of 284.6 eV. The measurement error is ±0.2 eV. The optical absorption properties of the samples were investigated through diffuse reflectance spectra (DRS) using a UV–vis spectrophotometer (Thermo Nicolet Evolution 500). Photoluminescence spectra (PL) of the samples were obtained using a fluorescence spectrometer (FLS-920) at 293 K, using a Xe lamp (excitation at 365 nm) as light source.

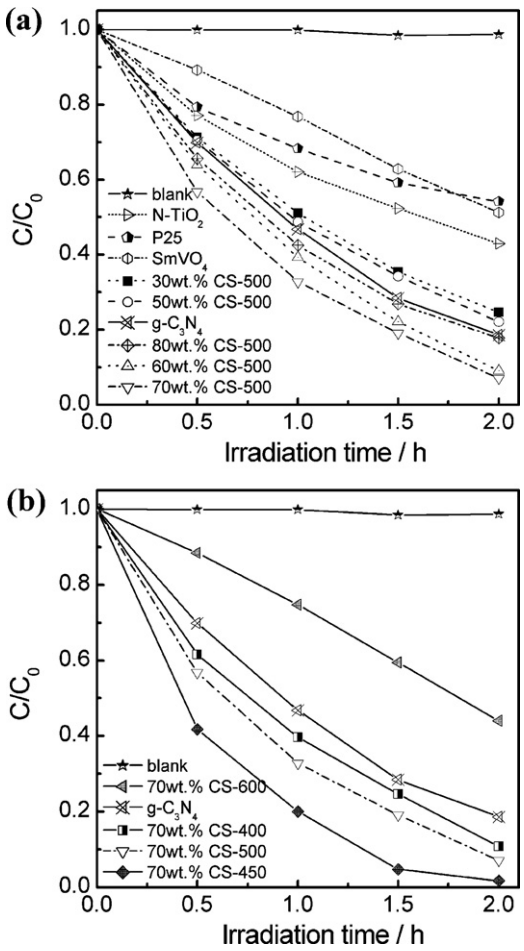

Fig. 1. Visible-light-driven photocatalytic activity of g-C_3N_4/$SmVO_4$ composites with different g-C_3N_4 concentration (a) and 70 wt.% g-C_3N_4/$SmVO_4$ samples calcined at different temperatures.

2.4. Photocurrent (PC) measurement

Photocurrent was measured on an electrochemical analyzer in a standard three-electrode system using the prepared samples as the working electrodes, a Pt wire as the counter electrode, and Ag/AgCl (saturated KCl) as a reference electrode. A 500 W Xe arc lamp through a UV-cutoff filter ($\lambda > 420$ nm) served as a light source. Na_2SO_4 (0.5 mol/L) aqueous solution was used as the electrolyte. Working electrodes were prepared as follows: an indium tin oxide (ITO) glass pieces with a size of 1.5 cm × 5 cm was cleaned successively by acetone, boiling NaOH (0.1 mol/L), deionized water, and then dried in an air stream. The electrically conductive adhesive with a size of 0.8 cm × 0.8 cm was pressed on the bottom center of ITO glass. Finally, the prepared powder was ground and closely compacted on the exposed electrically conductive adhesive.

3. Results and discussion

3.1. Photocatalytic activity of catalyst

RhB photocatalytic degradation was used to evaluate the photocatalytic activity of the g-C_3N_4/$SmVO_4$ composites. Simple RhB photolysis was also performed for comparison. The test result is shown in Fig. 1. The blank experiment in the absence of photocatalysts demonstrated that no RhB was photodegraded by the visible light. All the photocatalysts exhibited the photocatalytic activity in RhB degradation under visible light irradiation. $SmVO_4$ is an effective photocatalyst in photodegradation of acetone in gas phase [36]. However, the photocatalytic activity of $SmVO_4$ is low in the photodegradation of the RhB solution. P25 has a similar photoactivity as $SmVO_4$. Considering that P25 cannot absorb the light with $\lambda > 420$ nm, the observed activity can be attributed to the dye-sensitization effect. Moreover, the poor photocatalytic activity of P25 also indicates that the dye-sensitization effect contribution is limited in RhB degradation. N doping into TiO_2 greatly enhances the photoabsorption performance (see Fig. S1). Therefore, the photoactivity is increased. Pure g-C_3N_4 has a higher activity than $SmVO_4$ or N-TiO_2, which can be attributed to the moderate band gap and unique electronic structure of g-C_3N_4. With respect to the g-C_3N_4/$SmVO_4$ composites, the photocatalytic activity increases as g-C_3N_4 concentration increases from 30 wt.% to 70 wt.%, and decreases at an even higher g-C_3N_4 concentration. The highest photocatalytic activity is obtained from the catalyst 70 wt.% g-C_3N_4/$SmVO_4$ composite.

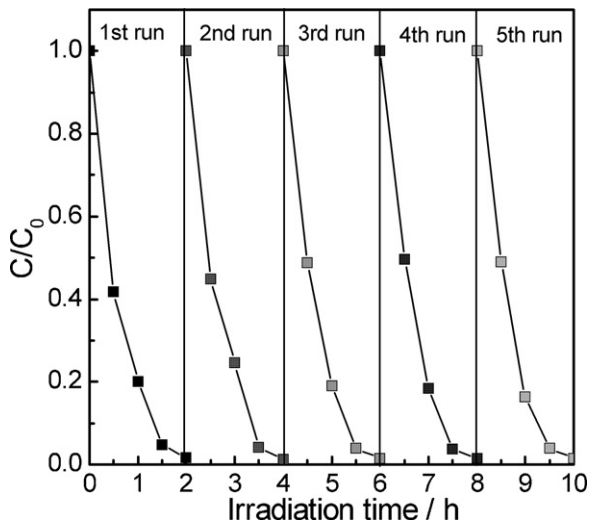

Fig. 2. Cycling runs for the photocatalytic degradation of RhB in the presence of 70 wt.% CS-450 sample under visible light irradiation.

Fig. 1b shows the photocatalytic activity of the 70 wt.% g-C_3N_4/$SmVO_4$ composites calcined at different temperatures. The calcination temperature greatly affects the catalyst activity. With the increase in temperature, the photocatalytic activity first increases and then quickly decreases. The photocatalyitc activity of the 70 wt.% CS-600 sample is as low as that of the pure $SmVO_4$. The sample calcined at 450 °C has the highest photocatalytic activity. The degradation rate reaches the maximum value of 2.07 h^{-1}, which is 2.4 and 4.6 times higher than those of the pure g-C_3N_4 and N-doped TiO_2, respectively (Fig. S2). The coupling of $SmVO_4$ and g-C_3N_4 creates a new visible-light-driven photocatalyst with high photocatalytic activity.

Although the g-C_3N_4/$SmVO_4$ composites exhibit higher photocatalytic activity, in view of practical applications, their stability is very important. Therefore, the cycling runs for RhB photodegradation using 70 wt.% CS-450 were performed to evaluate the photocatalytic stability of the g-C_3N_4/$SmVO_4$ composite. After every 2 h of photodegradation, the separated photocatalysts were washed with deionized water and dried. Fig. 2 shows the RhB decrease in every run. The photocatalytic activity does not exhibit any significant loss after five recycling runs. Aside from RhB, the g-C_3N_4/$SmVO_4$ composite also shows high photocatalytic activity for methylene blue (MB) photodegradation (Fig. S3). The MB dye-sensitization effect is lower than that of RhB. It indicates that the high photoactivity of the g-C_3N_4/$SmVO_4$ composite under visible light mainly originates from the coupled system itself. Therefore,

the g-C_3N_4/$SmVO_4$ composite has a promising practical application in water purification because of its high activity and stability.

3.2. BET analysis

To reveal the origin of the high activity of the g-C_3N_4/$SmVO_4$ composite, multiple techniques were applied to characterize the photocatalyst samples. Table 1 shows the specific surface areas of the different photocatalysts. The specific surface area of g-C_3N_4 is much lower than that of $SmVO_4$. The specific surface area of the g-C_3N_4/$SmVO_4$ composite calcined at 500 °C that has different g-C_3N_4 concentrations changes from 41 m^2/g to 79 m^2/g. No consistency between the BET value and the g-C_3N_4 concentration is observed. The change in the specific surface area does not match that in the catalyst activity. The specific surface area of the 70 wt.% g-C_3N_4/$SmVO_4$ composites calcined at different temperatures is also shown in Table 1. With the increase in calcination temperature, the BET value of the catalyst increased from 31 m^2/g to 47 m^2/g. However, no direct correspondence between the catalytic activity and the specific surface area exists. The sample calcined at 450 °C (51 m^2/g) is more active than that calcined at 400 °C (34 m^2/g) and 600 °C (71 m^2/g). Therefore, the data in Table 1 shows that the effect of specific surface area on catalytic activity is not the most important factor. The most important factor that affects the catalytic activity is the catalyst composition.

3.3. XRD, FT-IR analysis

The structure of the as-prepared g-C_3N_4/$SmVO_4$ composite was characterized by XRD. The results shown in Fig. 3 indicate that all the samples are well crystallized. The pure $SmVO_4$ is in its tetragonal phase (JCPDS 17-0876). The pure g-C_3N_4 presents two distinct peaks at 27.4° and 13.1°, which can be indexed as (0 0 2) and (1 0 0) diffraction planes (JCPDS 87-1526). With regard to the g-C_3N_4/$SmVO_4$ composite, both g-C_3N_4 and $SmVO_4$ can be detected with the exception of those in the 30 wt.% CS-500 sample. The non-detection of g-C_3N_4 in the 30 wt.% CS-500 sample may be due to its low g-C_3N_4 concentration. With the increase in the g-C_3N_4 concentration, the g-C_3N_4 XRD peak increases, whereas the $SmVO_4$ peaks decrease. No impurity phase was observed, indicating that the synthesized composite presents a two-phase composition, namely, g-C_3N_4 and $SmVO_4$. Fig. 3b shows the XRD patterns of the 70 wt.% g-C_3N_4/$SmVO_4$ samples calcined at different temperatures. The calcination temperature shows a great effect on the powder XRD patterns. When the calcination temperature is higher than 400 °C, the XRD peak of g-C_3N_4 decrease with the increase in calcination temperature and disappear at 600 °C. This result indicates that the heating process at high temperature decreases the g-C_3N_4 content, as proven by the TG–DTA experiment (Fig. 4). In Fig. 4, the TG–DTA curves of the pure g-C_3N_4 exhibit only one sharp weight loss with one endothermal peak at 743 °C in the temperature range of room temperature to 800 °C, which may be mainly attributed to the sublimation or decomposition of g-C_3N_4 since only a small amount of g-C_3N_4 was oxidized (Fig. S4). The TG–DTA curves of the physical mixture of $SmVO_4$ and g-C_3N_4 (70 wt.% CS-25) are highly different from those of pure g-C_3N_4. As shown in Fig. 4, two exothermal peaks at approximately 273 °C and 566 °C appear in the DTA curve of the 70 wt.% CS-25 sample, which may be due to the oxidation of g-C_3N_4. Correspondingly, two weight losses were observed in the TG curve. The total weight loss is 70 wt.%, indicating that only g-C_3N_4 is eliminated. The result in Fig. 4 clearly shows that the added $SmVO_4$ is a catalyst that can absorb and activate the oxygen in the air, and then oxidize the g-C_3N_4 at a relatively low temperature (Fig. S4) [37]. The high temperature can promote oxygen activation. Therefore, the decrease in g-C_3N_4 concentration is more evident in the sample calcined at a high temperature. When the mixture is calcined at

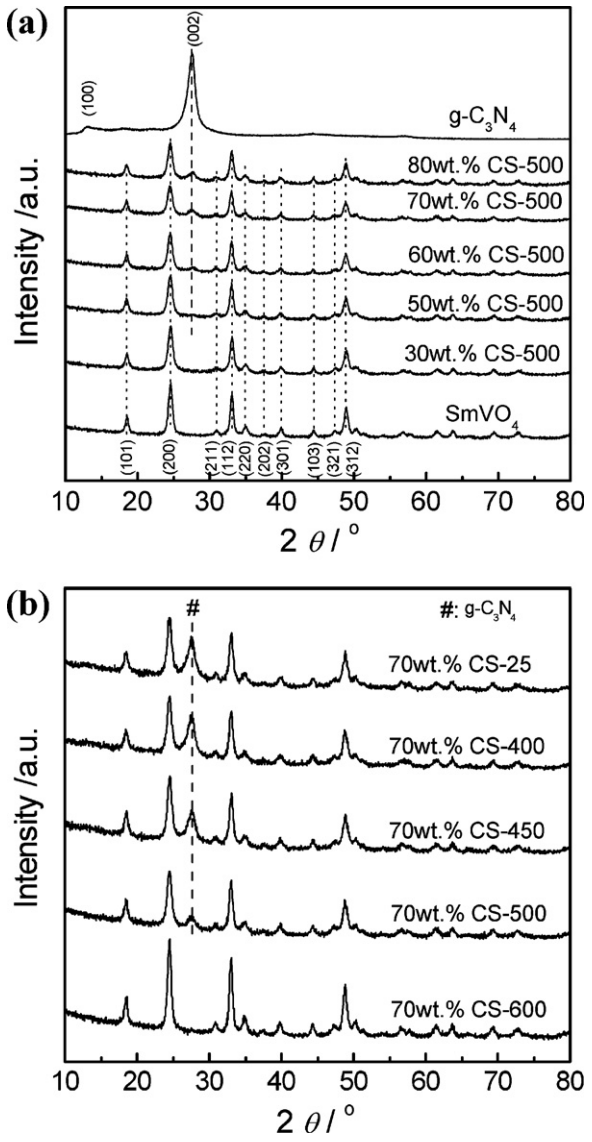

Fig. 3. XRD patterns of g-C_3N_4/$SmVO_4$ photocatalyst with different g-C_3N_4 concentration (a) and 70 wt.% g-C_3N_4/$SmVO_4$ samples calcined at different temperatures (b).

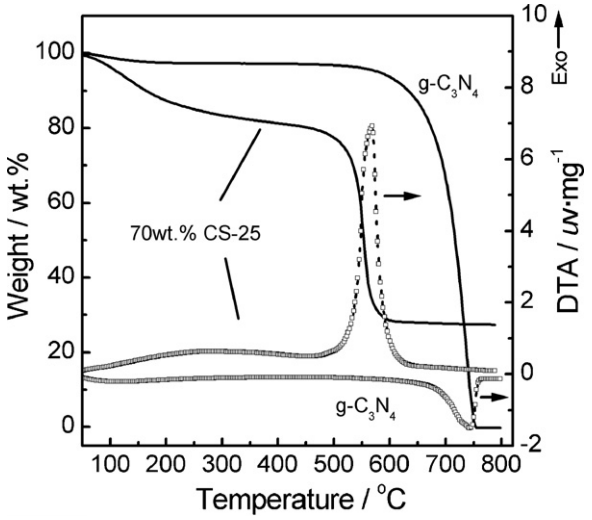

Fig. 4. TG–DTA thermograms for heating the pure g-C_3N_4 and 70 wt.% CS-25.

Table 1
Specific surface area and the real g-C_3N_4 concentration of g-C_3N_4/$SmVO_4$ composite photocatalysts.

Catalysts	S (m^2/g^1)	g-C_3N_4 content (wt.%)	Catalysts	S (m^2/g)	g-C_3N_4 content (wt.%)
g-C_3N_4	13	100	80 wt.% CS-500	56	42.1
$SmVO_4$	76	–	70 wt.% CS-25	31	70.3
30 wt.% CS-500	79	10.9	70 wt.% CS-400	34	65.8
50 wt.% CS-500	59	16.1	70 wt.% CS-450	51	50.5
60 wt.% CS-500	41	25.4	70 wt.% CS-600	71	–
70 wt.% CS-500	47	32.4			

600 °C, nearly all of g-C_3N_4 are eliminated and only $SmVO_4$ can be detected.

Besides the pure g-C_3N_4 and 70 wt.% CS-25 samples, the other g-C_3N_4/$SmVO_4$ composites were also characterized by TG–DTA experiment (Figs. S5 and S6). The result is shown in Table 1. The real g-C_3N_4 concentration is lower than the theoretical value for nearly all the g-C_3N_4/$SmVO_4$ composites (except the 70 wt.% CS-25 sample). With the increase in calcination temperature, the g-C_3N_4 concentration in the 70 wt.% g-C_3N_4/$SmVO_4$ composites decreases from 70.3 wt.% to 0, which agrees with the XRD result.

Fig. 5 shows the FT-IR spectra of the $SmVO_4$, g-C_3N_4, and g-C_3N_4/$SmVO_4$ composite photocatalysts. The peaks at 811 and 445 cm^{-1} in the $SmVO_4$ spectrum corresponds to the antisymmetrical stretching and deformation vibration of the VO_4 tetrahedra, respectively [38]. The broad peaks at 1641 and 3430 cm^{-1} may be due to the physically adsorbed water [39]. With regard to the pure g-C_3N_4, the peaks at 1251, 1325, 1419, 1571, and 1639 cm^{-1} correspond to the typical stretching modes of the CN heterocycles [17]. Additionally, the characteristic breathing mode of the triazine units at 810 cm^{-1} is observed [17]. The FT-IR spectra of g-C_3N_4/$SmVO_4$ depict the overlap of the FT-IR spectra of g-C_3N_4 and $SmVO_4$. With the increase in the g-C_3N_4 concentration or with the decrease of the calcination temperature, the FT-IR peaks of g-C_3N_4 increase. This result is consistent with that of the XRD experiment.

3.4. XPS analysis

Fig. 6 shows the XPS spectra of g-C_3N_4, $SmVO_4$, and the 70 wt.% g-C_3N_4/$SmVO_4$ samples calcined at different temperatures. Only one peak located at 284.6 eV was observed on the C 1s spectrum of the $SmVO_4$ sample. For the g-C_3N_4 sample, The C 1s spectra consist of two peaks. The peak at 284.6 eV, corresponding to C—C coordination, is due to carbon-containing contaminations, whereas the peak at 288.0 eV is related to the N—C—N coordination in the graphitic carbon nitride [40]. The g-C_3N_4/$SmVO_4$ composites also present two C 1s peaks, indicating the existence of graphitic carbon nitride. With the increase in calcination temperature, the peak at 288.0 eV is weakened and finally disappears in the 70 wt.% CS-600 sample. This occurrence is also observed in the N 1s peak at 398.6 eV, which is another characteristic peak of g-C_3N_4 [40]. Fig. 6c and d shows the V 2p and Sm 3d spectra of the different photocatalysts. The binding energy of V $2p_{3/2}$ is located at approximately 517.1 eV and barely changes in the different samples. This finding indicates that V^{5+} is present on the surfaces of these catalysts [41]. Similarly, the Sm valence state of the catalysts is +3 [42]. Thus, $SmVO_4$ is not reduced although it is a catalyst during the calcinations process. Only $SmVO_4$ and g-C_3N_4 can be detected on the surfaces of the composite photocatalysts.

3.5. SEM and TEM analysis

The morphologies of g-C_3N_4, $SmVO_4$, and the 70 wt.% CS-450 sample were characterized by SEM. As shown in Fig. 7, the $SmVO_4$ sample has aggregated particles that contain several smaller $SmVO_4$ crystals with approximately 50 nm diameters (Fig. 7a and b). Larger particles are observed in g-C_3N_4 (Fig. 7c and d). After introducing $SmVO_4$, the g-C_3N_4/$SmVO_4$ composite sample shows a similar morphology as that of pure $SmVO_4$ (Fig. 7e). This similarity in morphology of the g-C_3N_4/$SmVO_4$ composite sample to the pure $SmVO_4$ indicates that the aggregation of g-C_3N_4 is decreased greatly with the help of $SmVO_4$. An interaction between g-C_3N_4 and $SmVO_4$ exists. The chemical bond might be formed between the two semiconductors, which is beneficial for the charge transfer. Fig. 7f shows the TEM images of g-C_3N_4/$SmVO_4$ composite sample.

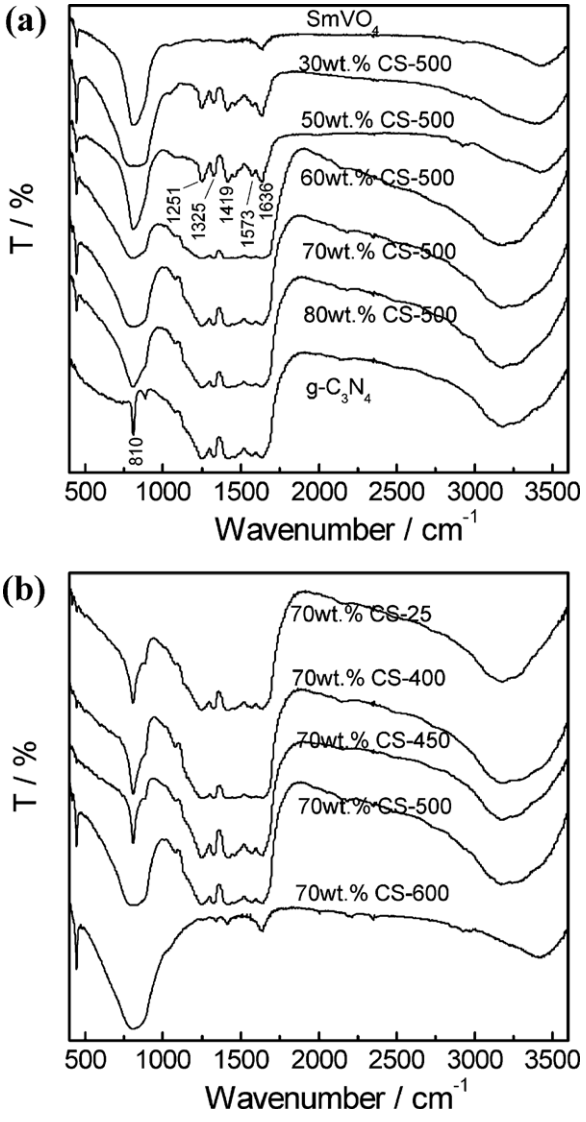

Fig. 5. FT-IR spectra of g-C_3N_4/$SmVO_4$ photocatalyst with different g-C_3N_4 concentration (a) and 70 wt.% g-C_3N_4/$SmVO_4$ samples calcined at different temperatures (b).

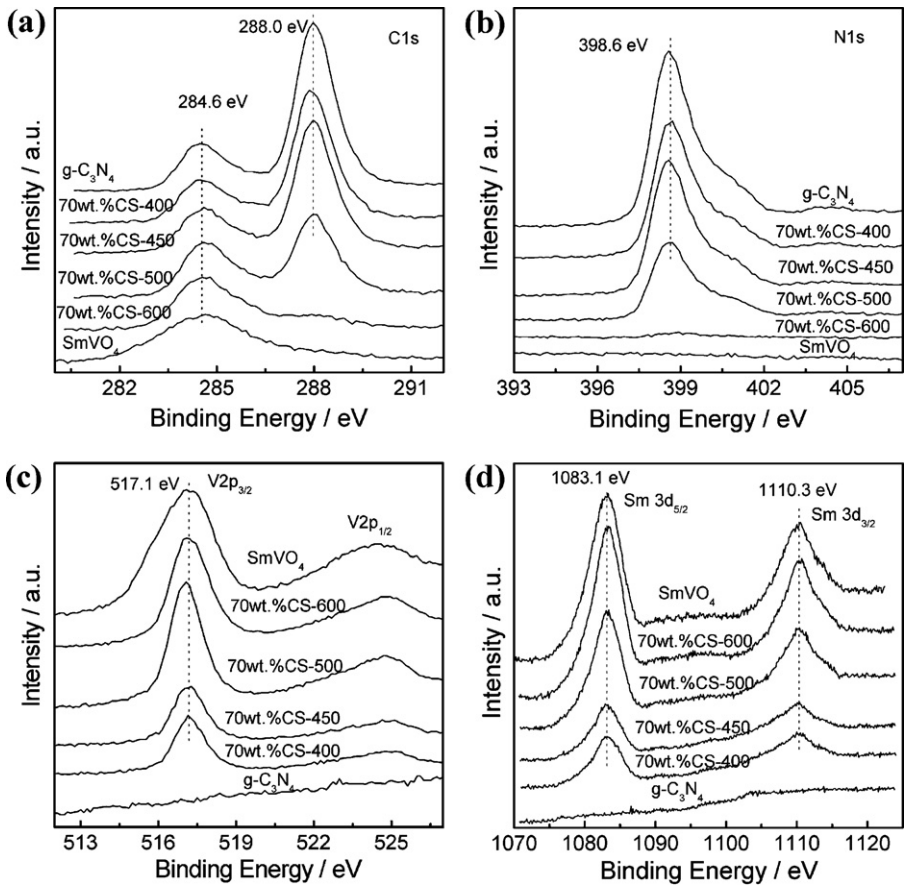

Fig. 6. XPS spectra of g-C_3N_4, $SmVO_4$, and 70 wt.% g-C_3N_4/$SmVO_4$ samples calcined at different temperatures: (a) C 1s, (b) N 1s, (c) V and (d) Sm.

$SmVO_4$ appears darker than g-C_3N_4 due to its higher atomic number. Moreover, $SmVO_4$ is finely dispersed on g-C_3N_4. The $SmVO_4$ particle size is between 30 nm and 60 nm, consistent with that in the SEM image.

3.6. DRS analysis

The optical absorption of the as-prepared g-C_3N_4/$SmVO_4$ samples was investigated using a UV–vis spectrometer. Fig. 8 shows that the $SmVO_4$ and g-C_3N_4 samples absorb UV to visible light, which signifies their visible-light-driven photocatalytic activities. Based on the Kubelka–Munk equation, the band gap of the two semiconductors can be deduced [34]. $SmVO_4$ has a band gap of 2.28 eV, while g-C_3N_4 has a band gap of 2.70 eV, both of which agree with the previous reported results [17,18]. Moreover, $SmVO_4$ exhibits a strong absorption at 300 nm. For g-C_3N_4, the strongest absorption peak is at 380 nm. The UV–vis spectra of the g-C_3N_4/$SmVO_4$ composite samples can be seen as the overlap of that of the consisting phases. With the increase in the $SmVO_4$ concentration or the calcination temperature, the peak at 300 nm increases at the expense of the peak at 380 nm, which is in good agreement with the XRD, FT-IR, and XPS results. However, the absorption edge of the composite barely changes, which suggests that the g-C_3N_4/$SmVO_4$ samples exhibit similar optical properties. Fig. 8d shows the valence-band X-ray photoelectron spectroscopy (VB XPS) spectrum of $SmVO_4$ and g-C_3N_4. The position of the valence band edge of g-C_3N_4 is located at approximately 1.50 eV, consistent with the results of Zou [21]. For $SmVO_4$, the value is approximately 1.99 eV. Using the equation of $E_{CB} = E_{VB} - E_g$, the CB edge potentials of the two semiconductors are also obtained. As shown in Fig. 9, the CB edge potential of g-C_3N_4 at −1.20 eV is more negative than that of $SmVO_4$ at −0.29 eV, whereas the VB edge potential of $SmVO_4$ at 1.99 eV is more positive than that of g-C_3N_4 at 1.50 eV. The suitable band potential indicates that the photoinduced electrons on the g-C_3N_4 particle surfaces can transfer easily to $SmVO_4$ via the well developed interface. Similarly, the photoinduced holes on the $SmVO_4$ surface can move to g-C_3N_4. This charge transfer would retard the electron–hole pair recombination and prolong the lifetime of charges, which is beneficial for the photocatalytic reaction.

3.7. PL and PC analysis

The catalyst characterization has proven that the g-C_3N_4/$SmVO_4$ composite is composed of $SmVO_4$ and g-C_3N_4. No impurity was observed in the bulk or on the catalyst surface. Moreover, it is widely accepted that the enhancement of photocatalytic performance of the composite photocatalyst is attributed to the efficient electron–hole pair separation. Therefore, it is reasonable that the charge transfer at the heterojunction interfaces of $SmVO_4$ and g-C_3N_4 is the most important factor affecting the photocatalytic activity, as shown in Fig. 9. However, this implication still needs proof. Therefore, photoluminescence analysis is used to reveal the efficiency of charge carrier trapping, transfer, and separation of the photogenerated electrons and holes in semiconductors. Fig. 10 shows the PL spectra of the g-C_3N_4 and g-C_3N_4/$SmVO_4$ catalysts. As can be seen from this figure, the PL spectrum of the g-C_3N_4/$SmVO_4$ composite is similar to that of pure g-C_3N_4. One main emission peak appears at approximately 460 nm, which is due to the band-band PL phenomenon with the light energy approximately equal to the band-gap energy of g-C_3N_4 [23]. The PL intensity of the

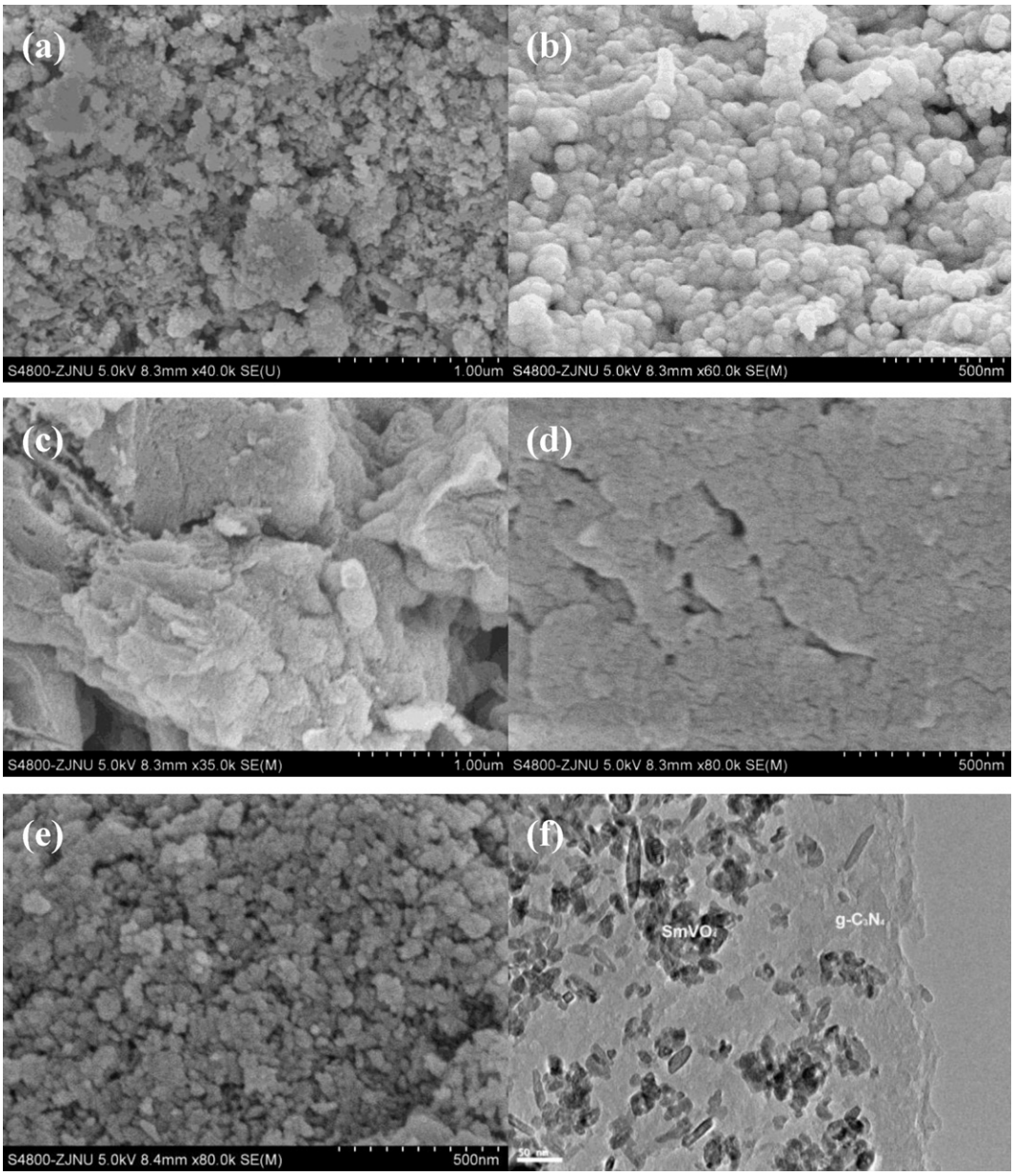

Fig. 7. SEM photograph of pure g-C_3N_4 (a and b) and $SmVO_4$ (c and d); SEM (e) and TEM (f) pictures of 70 wt.% CS-450 photocatalyst.

70 wt.% CS-450 composite is the lowest one. Considering that the PL emission results from the free charge carrier recombination, the lower peak indicates that the composite has a lower electrons and hole recombination rate under visible-light irradiation [43], which is mainly due to the fact that the electrons and holes are separated by the charge transfer at the heterojunction interfaces of $SmVO_4$ and g-C_3N_4.

To give further evidence to support the mechanism suggested above, photocurrent–time measurements were performed for a 250 s period under visible-light illumination in an on-and-off cycle mode. Fig. 11 shows the photocurrent–time curves of g-C_3N_4, $SmVO_4$, and the 70 wt.% CS-450 composite with two on–off intermittent irradiation cycles. The electrodes of the three samples demonstrate a rapid photocurrent response when the visible light illumination is on an on-and-off mode. The 70 wt.% CS-450 composite presents the highest photocurrent intensity, which is about three and seven times higher than that of g-C_3N_4 and $SmVO_4$. Presently, the photocurrent is widely regarded as the most efficient evidence demonstrating the charge separation in the composite photocatalysts [44,45]. A relationship is commonly recognized as follows: the higher the photocurrent, the higher the e^-–h^+ separation efficiency, and thus, the higher the photocatalytic activity. The result in Fig. 10 indicates that the composite has the lowest electrons-hole recombination rate, consistent with the PL and photocatalytic testing results.

Therefore, the high photocatalytic activity of the composite can be attributed to the g-C_3N_4 and $SmVO_4$ heterostructure, which enhances the photogenerated electron–hole pair separation. However, just like the other composite photocatalysts, the g-C_3N_4 content is pivotal in achieving the high photocatalytic activity of the g-C_3N_4/$SmVO_4$ composite. The suitable g-C_3N_4 concentration causes its good dispersion in the composite, which favors the formation of heterojunction structures between the g-C_3N_4 and $SmVO_4$ particles. Therefore, high separation of the charge carriers and photocatalytic activity are obtained on the 70 wt.% CS-500 sample. In addition to the g-C_3N_4 content, the contact between the

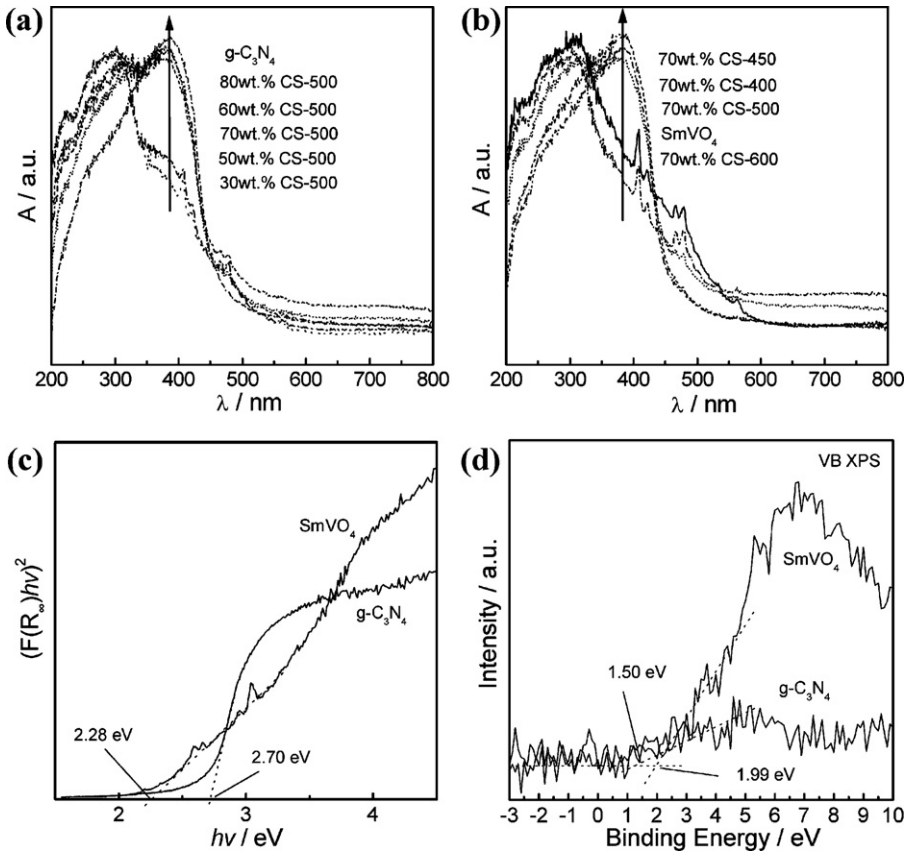

Fig. 8. UV–vis spectra of g-C_3N_4/$SmVO_4$ composites with different g-C_3N_4 concentration (a), 70 wt.% g-C_3N_4/$SmVO_4$ samples calcined at different temperatures (b), and estimated band gap of photocatalyst by Kubelka Munk function.

two semiconductors is also an important factor affecting the photocatalytic activity because the presence of the interface is needed to allow the highly efficient interparticle charge transfer. The poor contact between the two semiconductors would retard the charge transfer and decrease the separation efficiency [46]. Therefore, the uncalcined g-C_3N_4/$SmVO_4$ mixture has a similar photocatalytic activity as the pure g-C_3N_4 (Fig. S7). With the increase in calcination temperature, the chemical bond is formed between $SmVO_4$ and g-C_3N_4, which decreases the interface energy barrier and promotes the charge transfer. The lower electron–hole pair recombination and higher photocatalytic activity are thus obtained. However, the g-C_3N_4 concentration also changes with the increase in the calcination temperature due to the catalysis of $SmVO_4$. For example, the sample calcined at 600 °C contains no g-C_3N_4 phase and exhibits a similar photocatalytic activity as the pure $SmVO_4$. A suitable g-C_3N_4 concentration and a good interface are formed in the sample calcined at 450 °C. Therefore, the 70 wt.% CS-450 composite shows the highest photocatalytic activity under visible light irradiation.

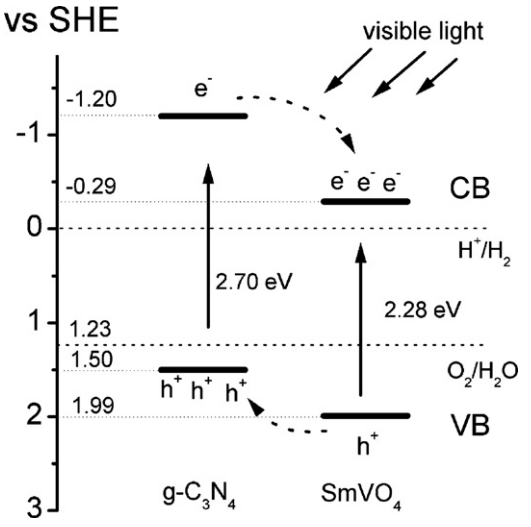

Fig. 9. Scheme for electron–hole separation and transport at the visible-light-driven g-C_3N_4/$SmVO_4$ composite photocatalyst interface.

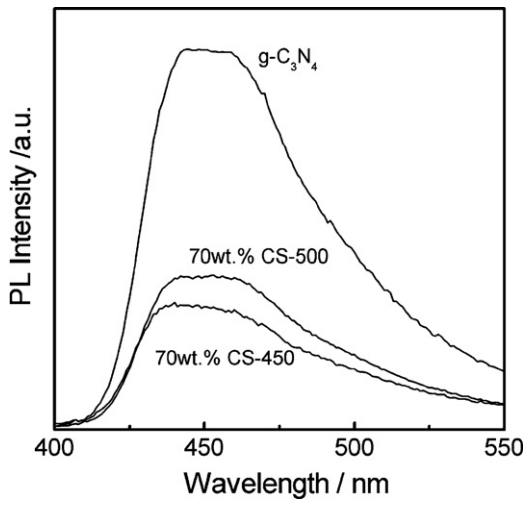

Fig. 10. Photoluminescence spectra of pure g-C_3N_4 and g-C_3N_4/$SmVO_4$ composite.

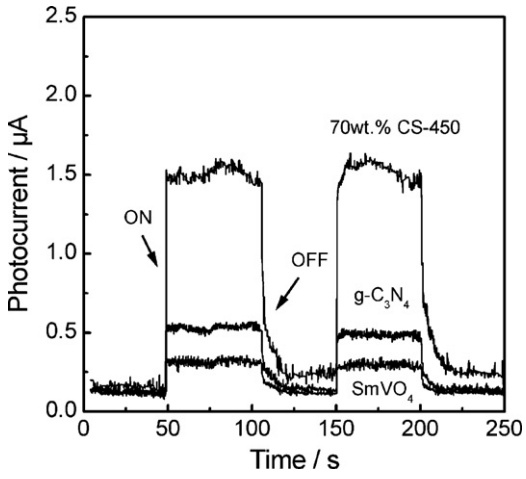

Fig. 11. Transient photocurrent response for $SmVO_4$, g-C_3N_4, and 70 wt.% CS-450 samples.

4. Conclusion

A series of g-C_3N_4/$SmVO_4$ composite photocatalysts with high visible light photocatalytic activity were prepared by the mixing–calcination method. The addition of g-C_3N_4 affects the textural properties and optical characteristics of $SmVO_4$. However, the high activity of g-C_3N_4/$SmVO_4$ composite is not attributed to these changes. The enhancement in activity may be due to the g-C_3N_4 and $SmVO_4$ heterostructure, which can induce high electron–hole pair separation. This supposition is proven by the PL and PC experiments. The g-C_3N_4 concentration and calcination temperature exert great effect on photocatalytic activity. The sample calcined at 450 °C and contained 50.3 wt.% g-C_3N_4 exhibits the highest photocatalytic activity with a degradation rate of 2.07 h^{-1}, which is 2.4 and 6.3 times higher than those of pure g-C_3N_4 and $SmVO_4$, respectively. This study demonstrates that g-C_3N_4 is a promising candidate for the development of high-performance and inexpensive photocatalysts with high visible-light photocatalytic activity

Acknowledgments

This work was supported by the National Natural Science Foundation of China (21003109) and the program for Zhejiang Leading Team of Science and Technology Innovation (2009R50020).

Appendix A. Supplementary data

Supplementary data associated with this article can be found, in the online version, at http://dx.doi.org/10.1016/j.apcatb.2012.09.031.

References

[1] X.B. Chen, S.H. Shen, L.J. Guo, S.S. Mao, Chemical Reviews 110 (2010) 6503–6570.
[2] D. Chatterjee, S. Dasgupta, Journal of Photochemistry and Photobiology C: Photochemistry Review 6 (2005) 186–205.
[3] M.N. Chong, B. Jin, C.W.K. Chow, C. Saint, Water Research 44 (2010) 2997–3027.
[4] W. Choi, A. Termin, M.R. Hoffmann, Journal of Physical Chemistry 98 (1994) 13669–13679.
[5] H. Yamashita, M. Harada, J. Misaka, M. Takeuchi, K. Ikeue, M. Anpo, Journal of Photochemistry and Photobiology A: Chemistry 148 (2002) 257–261.
[6] R. Ashi, T. Morikawa, T. Ohwaki, K. Aoki, Y. Taga, Science 293 (2001) 269–271.
[7] S. Sakthivel, H. Kisch, Angewandte Chemie International Edition 42 (2003) 4908–4911.
[8] T. Umebayashi, T. Yamaki, S. Tanaka, K. Asai, Chemistry Letters 32 (2003) 330–331.
[9] X. Chen, L. Liu, P.Y. Yu, S.S. Mao, Science 331 (2011) 746–750.
[10] G.H. Qin, Z. Sun, Q.P. Wu, L. Lin, M. Liang, S. Xue, Journal of Hazardous Materials 192 (2011) 599–604.
[11] P. Wang, B.B. Huang, X.Y. Zhang, X.Y. Qin, H. Jin, Y. Dai, Z.Y. Wang, J.Y. Wei, J. Zhan, S.Y. Wang, J.P. Wang, M.H. Whangbo, Chemistry: A European Journal 15 (2009) 1821–1824.
[12] J. Zhang, F.J. Shi, J. Lin, D.F. Chen, J.M. Gao, Z.X. Huang, X.X. Ding, C.C. Tang, Chemistry of Materials 20 (2008) 2937–2941.
[13] Z.G. Yi, J.H. Ye, N. Kikugawa, T. Kako, S.X. Ouyang, H. Stuart-Williams, H. Yang, J.Y. Cao, W.J. Luo, Z.S. Li, Y. Liu, R.L. Withers, Nature Materials 9 (2010) 559–564.
[14] M. Hara, G. Hitoki, T. Takata, J.N. Kondo, H. Kobayashi, K. Domen, Catalysis Today 78 (2003) 555–560.
[15] Y.J. Wang, Y.M. He, T.T. Li, J. Cai, M.F. Luo, L.H. Zhao, Catalysis Communications 18 (2012) 161–164.
[16] Y.P. Bi, S.X. Ouyang, N. Umezawa, J.Y. Cao, J.H. Ye, Journal of the American Chemical Society 133 (2011) 6490–6492.
[17] S.C. Yan, Z.S. Li, Z.G. Zou, Langmuir 25 (2009) 10397–10401.
[18] G.Q. Li, N. Yang, W.L. Wang, W.F. Zhang, Journal of Physical Chemistry C 113 (2009) 14829–14833.
[19] G. Liu, P. Niu, C.H. Sun, S.C. Smith, Z.G. Chen, G.Q. Lu, H.M. Cheng, Journal of the American Chemical Society 132 (2010) 11642–11648.
[20] Y.J. Zhang, A. Thomas, M. Antonietti, X.C. Wang, Journal of the American Chemical Society 131 (2009) 50–51.
[21] S.C. Yan, S.B. Lv, Z.S. Li, Z.G. Zou, Journal of the Chemical Society: Dalton Transactions 39 (2010) 1488–1491.
[22] Y. Liu, G. Chen, C. Zhou, Y.D. Hu, D.G. Fu, J. Liu, Q. Wang, Journal of Hazardous Materials 190 (2011) 75–80.
[23] L. Ge, C.C. Han, J. Liu, Applied Catalysis B: Environmental 108–109 (2011) 100–107.
[24] M.D. Guo, A.T. Aldred, S.K. Chan, Journal of Physics and Chemistry of Solids 48 (1987) 229–235.
[25] B.C. Chakoumakos, M.M. Abraham, L.A. Boatner, Journal of Solid State Chemistry 109 (1994) 197–202.
[26] L. Chen, Materials Letters 60 (2006) 1859–1862.
[27] B.P. Barbero, L.E. Cadus, Applied Catalysis A: General 234 (2002) 245–258.
[28] S. Mahapatra, G. Madras, T.N. Guru Row, Industrial and Engineering Chemistry Research 46 (2007) 1013–1017.
[29] Y.M. He, Y. Wu, T.L. Sheng, X.T. Wu, Journal of Hazardous Materials 180 (2010) 675–682.
[30] Y.M. He, Y. Wu, H. Guo, T.L. Sheng, X.T. Wu, Journal of Hazardous Materials 169 (2009) 855–860.
[31] H.J. Huang, D.Z. Li, Q. Li, W.J. Zhang, Y. Shao, Y.B. Chen, M. Sun, X.Z. Fu, Environmental Science and Technology 43 (2009) 4164–4168.
[32] Y.M. He, Y.J. Wang, L.H. Zhao, X.T. Wu, Y. Wu, Journal of Molecular Catalysis A: Chemical 337 (2011) 61–67.
[33] N.C. Castillo, A. Heel, T. Graule, C. Pulgarin, Applied Catalysis B: Environmental 95 (2010) 335–347.
[34] M. Long, W. Cai, J. Cai, B. Zhou, X. Chai, Y. Wu, Journal of Physical Chemistry B 110 (2006) 20211–20216.
[35] S. Eda, M. Fujishima, H. Tada, Applied Catalysis B: Environmental 125 (2012) 288–293.
[36] Y.M. He, T.L. Sheng, J.S. Chen, R.B. Fu, S.M. Hu, X.T. Wu, Catalysis Communications 10 (2009) 1354–1357.
[37] B.P. Barbero, L.E. Cadus, Applied Catalysis A: General 237 (2002) 263–273.
[38] Z.M. Fang, Q. Hong, Z.H. Zhou, S.J. Dai, W.Z. Weng, H.L. Wan, Catalysis Letters 61 (1999) 39–44.
[39] A.M. Efimov, V.G. Pogareva, Chemical Geology 229 (2006) 198–217.
[40] H.J. Yan, Y. Chen, S.M. Xu, International Journal of Hydrogen Energy 37 (2012) 125–133.
[41] Y.H. Zhu, W.M. Lu, H. Li, H.L. Wan, Journal of Catalysis 246 (2007) 382–389.
[42] P.J. Tian, J.S. Cheng, G.K. Zhang, Applied Surface Science 257 (2011) 4896–4900.
[43] F.B. Li, X.Z. Li, Applied Catalysis A: General 228 (2002) 15–27.
[44] M. Kong, Y.Z. Li, X. Chen, T.T. Tian, P.F. Fang, F. Zheng, X.J. Zhao, Journal of the American Chemical Society 133 (2011) 16414–16417.
[45] Q.J. Xiang, J.G. Yu, M. Jaroniec, Journal of Physical Chemistry C 115 (2011) 7355–7363.
[46] X.P. Lin, F.Q. Huang, J.C. Xing, W.D. Wang, F.F. Xu, Acta Materialia 56 (2008) 2699–2705.